INL/JOU-21-62454-Revision-0

BISON Fuel Performance Modeling Optimization for Experiment X447 and X447A Using Axial Swelling and Cladding Strain Measurements

August 2022

Kyle Mitchell Paaren, Ammon Hughes Black, Nancy J Lybeck, Kun Mo, Benjamin W Spencer, Pavel G Medvedev, Douglas L Porter

Changing the World's Energy Future

Idaho National Laboratory

INL/JOU-21-62454-Revision-0

BISON Fuel Performance Modeling Optimization for Experiment X447 and X447A Using Axial Swelling and Cladding Strain Measurements

Kyle Mitchell Paaren, Ammon Hughes Black, Nancy J Lybeck, Kun Mo, Benjamin W Spencer, Pavel G Medvedev, Douglas L Porter

August 2022

Idaho National Laboratory
Idaho Falls, Idaho 83415

http://www.inl.gov

Prepared for the
U.S. Department of Energy
Under DOE Idaho Operations Office
Contract DE-AC07-05ID14517

BISON Fuel Performance Modeling Optimization for Experiment X447 and X447A Using Axial Swelling and Cladding Strain Measurements

Kyle M. Paaren*[,a] (kyle.paaren@inl.gov), Ammon Black[a] (ammon.black@inl.gov), Nancy Lybeck[a] (nancy.lybeck@inl.gov), Kun Mo[b] (kunmo@anl.gov), Benjamin W. Spencer[a] (benjamin.spencer@inl.gov), Pavel Medvedev[a] (pavel.medvedev@inl.gov), and Douglas Porter[a] (douglas.porter@inl.gov)

[a] *Idaho National Laboratory: 2525 Fremont Ave., Idaho Falls, Idaho, 83415*
[b] *Argonne National Laboratory: 9700 S Cass Ave., Lemont, IL 60439*

*Corresponding Author

ABSTRACT

With the recent need to qualify new reactor designs, such as the Versatile Test Reactor, researchers need fuel performance calculations to determine the safety criteria of proposed designs. In order to validate the fuel performance results obtained by the fuel performance code BISON for new reactor designs, legacy fuel from EBR-II and Fast Flux Test Facility MFF with post-irradiation examination (PIE) data need to be used as validation cases to benchmark models. In this work, BISON has been paired with the Fuels Irradiation & Physics Database (FIPD) and the Integral Fast Reactor Materials Information System (IMIS) to supply PIE data for comparison with simulations of EBR-II experiments X447/X447A. X447/X447A were assessed by implementing models for a fuel-cladding chemical interaction (FCCI) within BISON and optimizing the friction coefficient between the fuel surface and the cladding, the anisotropic swelling factor, and the HT9 first thermal creep scalar (which scales the first term in the HT9 creep equation) to best match the PIE axial fuel swelling height and cladding profilometry for all pins in X447/X447A. The optimal values were found using a generic algorithm developed to select different values for the three parameters until end criteria was met and error couldn't be reduced further. The BISON-simulated cladding profilometry was evaluated using a standard error of the estimate to account for the profile shape of the cladding profilometry. Optimal values for the friction coefficient, anisotropic fuel swelling factor, and HT9 first thermal creep scalar were found to best fit the BISON simulation results to the PIE measurements found in IMIS and FIPD. Possible improvements to current models to account for the underprediction of fuel swelling at low burnups and the overprediction of fuel swelling at higher burnups that is observed for the axial fuel swelling height are discussed. Although two pins in EBR-II, X447/X447A (DP70 and DP75), were known to fail due to FCCI, none of the pins simulated in BISON reached a cumulative damage fraction above 0.008 with FCCI correlations coupled in the BISON simulations. The error estimate generated for all pins in X447/X447A using optimal values was 209 μm, which is deemed acceptable.

KEYWORDS
BISON
Simulation
Finite Element Method
EBR-II
Automation
Metallic Fuel

ABREVIATIONS

ALFUS	Alloy Fuel Unified Simulator
ANL	Argonne National Laboratory
CCCI	cladding coolant chemical interaction
CDF	cumulative damage fraction
CDM	continuum damage mechanics
EBR-II	Experimental Breeder Reactor II
FCCI	fuel cladding chemical interaction
FCMI	fuel cladding mechanical interaction
FGR	fission gas release
FIPD	Fuels Irradiation & Physics Database
IMIS	Integral Fast Reactor Materials Information System
LHGR	linear heat generation rate
MOOSE	Multiphysics Object Orientated Simulation Environment
MF	mutation factor

PIE post-irradiation examination
SEE standard error of the estimate
VTR Versatile Test Reactor

1. INTRODUCTION

In recent years, a renewed interest in designing next generation reactors has spurred the development of new nuclear fuels as well as reactors to test these fuels. The Versatile Test Reactor (VTR) will provide the necessary tests for next generation reactors, such as molten-salt reactors, gas-cooled fast reactors, and sodium-cooled fast reactors [1]. Metallic fuels are of interest for testing in the VTR system due to current customer designs, such as those of TerraPower. The VTR design criteria dictate that an acceptable failure criterion is that no more than one pin in 13,000 fail [1]. In order to achieve this design criterion, it is important to provide appropriate simulations with a fuel performance code, such as BISON [2]. To prepare BISON to help the VTR and other next generation reactor testing programs, BISON has been paired with the Fuels Irradiation & Physics Database (FIPD) and Integral Fast Reactor Materials Information System (IMIS), which supply post-irradiation examination (PIE) and fuel pin data from Experimental Breeder Reactor (EBR) II. With the databases linked to BISON, proper assessment cases can be used to validate metallic fuel models within the BISON code. This work attempts to replicate the behavior of the X447 and X447A EBR-II experiments, with a focus on capturing frictional contact and fuel-cladding chemical interaction (FCCI) effects by statistically fitting BISON simulation results to PIE cladding profilometry and fuel axial swelling. A failure indicator known as the cumulative damage fraction (CDF) is also computed in BISON and compared against pins DP70 and DP75, which were known to fail due to FCCI.

Prior work in BISON job submission automation will be used extensively in the scope of this work [3][4]. This work showed the coupling of IMIS and FIPD to perform fuel performance analyses of EBR-II metallic fuel pins with BISON. These simulations included using frictional contact, pin-specific power and flux histories, pin-specific axial power and axial flux profiles, and irradiation-induced volumetric swelling of the cladding material [4][5]. PIE cladding profilometries for HT9, D9, and SS316 agreed with BISON results under the pin temperatures of experiments X421/X421A, X441/X441A, and X486. While some swelling may occur in HT9, it was considered negligible in prior codes, such as the Alloy Fuel Unified Simulator (ALFUS) [3]. For experiment X447/X447A, the assembly flowrate was reduced to produce higher fuel and cladding temperatures. Due to the elevated temperatures of the HT9 cladding in X447/X447A, FCCI occurs at a non-negligible rate and wasn't accounted for in previous modeling efforts. FCCI thins out the interior cladding wall, allowing for more thermal creep and cladding strain as a result [6][7]. This ultimately leads to the failure of the HT9 clad pins, DP70 and DP75 in X447, due to excessive strain.

An FCCI model from the LIFE-METAL fuel performance code has been previously implemented into BISON to estimate the wastage thickness formed on the interface between the metallic fuel and the cladding interior surface. It allows for the wastage to be calculated using time-at-temperature and either flux, burnup, or a combination of the two for HT9, D9, and SS316 cladding. These correlations are seen in Equations 1–3, with the coefficients fitted based on PIE data from EBR-II experiments. Within Equations 1–3, ϕ is neutron flux, B is the at.% burnup, R is the gas constant, T is temperature in Kelvin, and D_0, Q, k_0, and D_{i0} are empirical constants. The flux mode was calibrated using experiments X419, X420, X421, X425, X429, X441, and X447, where the burnup and flux-burnup modes were calibrated using only experiment X447 [8][9]. A similar model for cladding coolant chemical interaction (CCCI) has previously been implemented in BISON as well to further account for the thinning of the cladding material. However, neither of these models had been used in the BISON code to capture the effect of the thinning of the cladding wall on the mechanical response. This work couples the wastage formed into the BISON mechanical simulations.

FCCI Flux Dependent
$$\frac{\Delta w}{\Delta t} = \frac{1}{2}\left(D_0 e^{-\frac{Q}{RT}} + D_{i0}\phi\right)^{\frac{1}{2}} t^{\frac{-1}{2}} \quad (1)$$

FCCI Burnup Dependent
$$\frac{\Delta w}{\Delta t} = 2B\left(k_0 e^{-\frac{Q_b}{RT}}\right) t^{\frac{-1}{2}} \quad (2)$$

FCCI Flux-Burnup Dependent
$$\frac{\Delta w}{\Delta t} = 2B\left(D_0 e^{-\frac{Q}{RT}} + D_{i0}\phi\right)^{\frac{1}{2}} t^{\frac{-1}{2}} \quad (3)$$

PIE measurements from IMIS and FIPD include burnup calculations, cladding profilometry, and fuel axial swelling from a variety of EBR-II experiments, including X447/X447A. Previous BISON simulations, particularly cladding profilometry results, were compared to PIE measurements to validate irradiation-induced volumetric void swelling models for cladding materials [4]. The implementation of these models significantly improved the BISON profilometry predictions for D9 and

SS316 cladding materials. However, fuel-cladding mechanical interaction (FCMI) played a significant role when gas-generated fuel swelling in BISON was implemented. The BISON gaseous fission product swelling model overpredicts the total swelling of the fuel with the FCMI contact method, fuel terminating porosity (where gaseous bubbles interconnect), and anisotropic fuel swelling factor determining the amount of volumetric swelling the fuel undergoes, and the anisotropic nature of the swelling. The amount of volumetric swelling of the metallic fuel and the direction of the swelling determines the amount of cladding strain produced from FCMI. The elevated temperatures in X447/X447A allow for more thermal creep to occur, which is accelerated by FCCI and CCCI. This work seeks to match the profilometry data generated by BISON and fit it to the profilometry data supplied by FIPD and IMIS for subassembly X447/X447A in EBR-II. The intent is to produce results that closely match the reality of experiment X447/X447A using the current BISON models by optimizing the anisotropic swelling factor and friction coefficient used for contact.

2. METHODS

This work builds on the approach for simulating the thermomechanical response of metallic fuels used by the BISON code, which is summarized in Section 1. This work attempts to optimize the friction coefficient used in the contact model, the anisotropic swelling factor within gaseous fission product swelling material model, and the first thermal scalar within the HT9 creep equation. This was to best fit the PIE cladding profilometry and axial fuel swelling measurements to the BISON results. Coupling FCCI and CCCI into the BISON code was also done to evaluate the X447/X447A profilometry due to the known elevated temperatures. The genetic algorithm used to minimize errors between simulation and experimental data focused on model parameters for swelling, frictional contact, cladding creep, and wastage thinning. Details of the models whose parameters were adjusted are provided in the following sections.

2.1 General Solution Approach

The metallic fuel response is simulated using the BISON fuel performance code. The BISON input files are created with an automated system by modifying a generic EBR-II input file used in previous work [3][4]. The fuel performance calculations for the X447/X447A experiments include the mechanical and thermal contact between the fuel surface and the inner cladding wall to simulate FCMI and provide heat transfer to the sodium coolant. Geometric dimensions, initial conditions, boundary conditions, and power and flux histories from each pin from X447/X447A were supplied from IMIS and FIPD to be used in conjunction with material models and contact actions within BISON [3][4]. Material models within BISON allow for different phenomena within the simulations to be incorporated into material properties, such as burnup, porosity, fission gas release, void swelling, and FCCI [2][10]. This work builds on fully coupled EBR-II simulations to incorporate cladding thinning due to FCCI and to optimize three parameters that contribute to cladding strain at elevated temperatures. The coupling of material models used to describe material properties for the fuel and the cladding are listed in Table 1 with the corresponding BISON object. The interconnection of the models is shown in Figure 1 to include FCCI.

Table 1. BISON Objects used in BISON Simulations

Phenomenon and Property	Fuel	Cladding
Fuel Phase	PhaseUPuZr [11]	N/A
Thermal Conductivity	ThermalUPuZr [12][13]	ThermalHT9 [5][14] ThermalD9 [5][15][16] Thermal316 [17]
Density ($g \cdot cm^{-3}$)	15.8	7.8
Burnup	UPuZrBurnup [18]	N/A
Fission Rate	UPuZrFissionRate [8]	N/A
Elasticity Tensor	UPuZrElasticityTensor [5]	HT9ElasticityTensor [19] D9ElasticityTensor [5]
Creep	UPuZrCreepUpdate [5]	HT9CreepUpdate [5] D9CreepUpdate [5]
Thermal Expansion	UPuZrThermalExpansionEigenstrain [20]	HT9ThermalExpansionEigenstrain [16] D9ThermalExpansionEigenstrain [5][16]
Gaseous Swelling	UPuZrGaseousEigenstrain [18][21]	N/A
Fission Gas Release	UPuZrFissionGasRelease [22]	N/A
Solid Swelling	BurnupDependentEigenstrain [23]	N/A

Cladding Void Swelling	N/A	HT9VolumetricSwellingEigenstrain [5] D9VolumetricSwellingEigenstrain [5]
FCCI	N/A	MetallicFuelWastage [8] MetallicFuelWastageDamage [8]
CDF	N/A	FailureCladHT9 [24] FailureCladD9 [25]

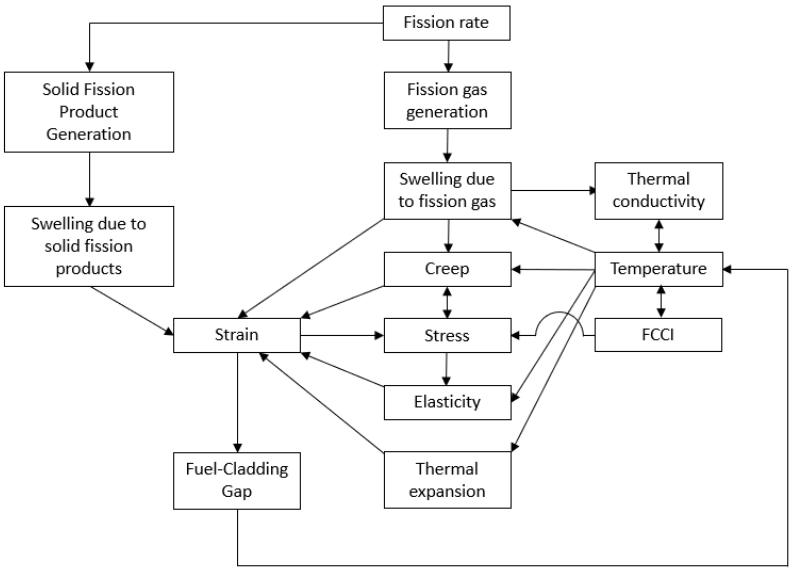

Figure 1. Coupling of BISON variables and material properties.

2.2 Swelling Model

The BISON gaseous fission product swelling model calculates the relative amounts of radial and axial swelling the U-Pu-Zr fuel experiences. The applied eigenstrain tensor is shown in Equation 4, where the eigenstrain ϵ_{ij} is a function of the volumetric swelling and an identity matrix modified by the anisotropic swelling factor f [8]. The anisotropic factor's current default value in BISON is set to 0 but can be modified to values from –1 to 1. In this work, the anisotropic factor is optimized to produce the best fit to the profilometry results by examining anisotropic swelling factor values between 0 and 1, as previous literature has suggested values between 0.25–0.7 depending on plutonium content [21]. Although literature suggests the anisotropic swelling factor is between 0.25-0.7, the purpose behind the anisotropic swelling factor is meant as a proportionality constant to represent phenomena not yet explained through mechanistic modeling, which is why the value was allowed to exist between 0 and 1 [21]. This eigenstrain is subtracted from the strain computed from the mechanical deformation prior to an evaluation of the constitutive model that computes the stress.

Modified U-Pu-Zr Eigenstrain

$$\epsilon_{ij} = \left(\frac{\Delta V}{V_0}\right)_g \begin{bmatrix} 1+f & 0 & 0 \\ 0 & 1-2f & 0 \\ 0 & 0 & 1+f \end{bmatrix} \quad (4)$$

The maximum amount of volumetric swelling of the U-Pu-Zr fuel is determined by the initial porosity of the fuel and the terminating porosity [8], as shown in Equation 5. The total volumetric eigenstrain from gaseous swelling is fixed by the terminating porosity, with the direction of the eigenstrain being controlled by the anisotropic factor. However, the contact method chosen for FCMI can influence the direction of the swelling by binding the direction the U-Pu-Zr fuel matrix creeps. Although the U-Pu-Zr creep equation proportionality constants could have been adjusted to indirectly control the direction of swelling, other models within BISON utilize stress, which is dependent on creep. The contact method within BISON controls the friction coefficient used for FCMI. The BISON defaults for terminating porosity caused an over swelling of the EBR-II fuel for 75% smeared density pins in preliminary results [3][4]. To account for this, other codes, such as ALFUS, have implemented a hot pressing component for U-Pu-Zr fuel to account for the excess volumetric strain [23]. It was determined

that 75% smeared density EBR-II fuel pins had a volumetric strain of 34% for burnup values between 2–10 at.%, accounting for gaseous swelling, solid fission product swelling, and hot pressing of the U-Pu-Zr fuel [23]. To achieve this in the X447/X447A simulations, an initiating porosity and terminating porosity of 0.17 and 0.19, respectively, were supplied within UPuZrGaseousEigenstrain. The initiating porosity control when FGR begins, with terminating porosity determining when pores are interconnected, preventing further swelling from gaseous fission products. The initial porosity was provided as zero, although fresh EBR-II fuel had a density of 15.7 g·cm^{-3}, with the theoretical density being 16.2 g·cm^{-3}. Although the initial porosity could have been set to 3.185% to account for the density difference, the initial porosity would only slightly change the porosity correction in the thermal conductivity model and fuel elasticity matrix. The initial porosity does not affect the volumetric swelling of the fuel, as that is based on the porosity change.

Maximum U-Pu-Zr Swelling $$\left(\frac{\Delta V}{V_0}\right)_g^{max} = \frac{p_{term} - p_{initial}}{1-(p_{term} - p_{initial})} \quad (5)$$

2.3 Frictional Contact Model and Creep Model Parameter

During the optimization phase, the friction coefficient was restricted to values between 0 and 1, with the first thermal scalar of the HT9 creep equation bound between 1 and 20. These boundaries were chosen due to unrealistic nature and overprediction of cladding strain for lower temperature pins with HT9 first thermal scalar values above 20. For the friction coefficient, this was particularly important as there are multiple BISON friction models that affect the output of the BISON simulation. Frictional contact between the fuel and the cladding was chosen as it represents realistic physics compared to frictionless contact used in assessment cases which providing the same cladding strain as glued contact. This is important to model, as EBR-II rods examined during PIE were welded to the inner cladding surface. The friction model used in this study was a coulomb model with AugmentedLagrangian as the contact solver. AugmentedLagrangian was chosen over other contact methods in BISON due to it being more robust with oscillating pin power histories with frictional contact. Frictional contact was used to bind the U-Pu-Zr fuel matrix from creep axially up the inner cladding wall, leading to the overprediction of axial fuel swelling height. The first thermal scalar of the HT9 creep equation was varied by increments of one, as the implementation of FCCI was not sufficient for the BISON simulations to match the X447/X447A profilometry. The HT9 thermal creep equation is seen below in Equation 6, where γ is the HT9 first thermal creep scalar, σ is the effective stress in MPa, and T is the temperature in Kelvin [5].

HT9 Thermal Creep $$\dot{\epsilon}_{thermal} = \gamma * 1.17 * 10^9 e^{\frac{-83142}{RT}} \sigma^2 + 8.33 * 10^9 e^{\frac{-108276}{RT}} \sigma^5 \quad (6)$$

Previous modeling attempts of experiments X447/X447A have been ineffective in replicating the spike in cladding strain near the top of the EBR-II fuel pin that is not present in other EBR-II experiments, such as X441/X441A, that contain the same burnup, fuel composition, and cladding. The fundamental difference between X441/X441A and X447/X447A is a reduced coolant flowrate, which leads to elevated temperatures within the fuel, cladding, and coolant [26][27]. The increase in temperatures leads to more thinning of the cladding material by wastage [6][7]. The thinning of the cladding material from FCCI leads to higher stress and thermal creep near the region of the cladding near the top of the U-10Zr fuel. This is seen by contrasting the cladding profilometries of X441A and X447A with the same fuel smeared density, cladding outer diameter, cladding material, and similar burnups in Figure 2. The X447A cladding temperatures were much hotter than in X441A. Due to cladding wastage thickness calculated in BISON being in agreement with FCCI wastage PIE measurements, proportionality constants within the FCCI wastage model were not adjusted, leaving proportionality constants within the HT9 thermal creep equation to be adjusted to match the PIE measurements [6].

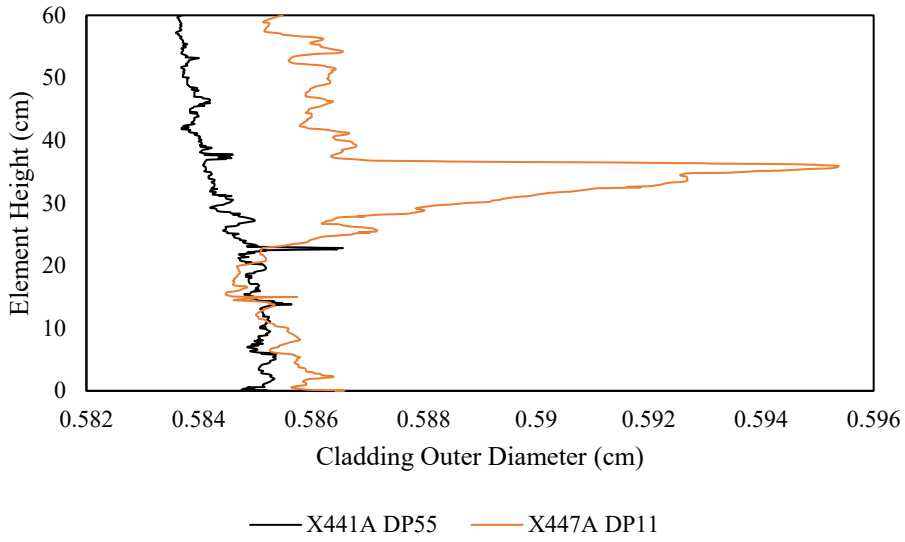

Figure 2. Cladding PIE profilometry comparison between X441A DP55 (10.0 at. % BU) and X447A DP11 (8.9 at. % BU).

2.4 Wastage Thinning Model

Previous FCCI modeling efforts in BISON calculated the wastage thinning of the cladding material based on burnup, neutron flux, and time-at-temperature [8][9]. However, the effect of the wastage thinning of the cladding material was not accounted for in the computation of the mechanical response until recently. This thinning should result in higher stress and increased thermal creep. Thinning could be represented in the computational model by modifying the physical thickness of the wall, which could be accomplished in a number of ways, including modifying the finite element mesh or using immersed boundary methods to represent a moving domain boundary within a fixed mesh. However, these techniques introduce significant complexity to an already challenging problem, so a simpler solution was sought. The theory of continuum damage mechanics (CDM), which is widely used to model the effects of fracture on the mechanical response of materials, provides a convenient framework for representing the thinning effect and is employed here from the Multiphysics Object Orientated Simulation Environment (MOOSE) [28][29].

The basic premise of CDM is that material damage is manifested as a reduction in the effective area of a cross section of a representative volume element due to void growth, microcracking, or other similar phenomena. The damage results in a reduction in the effective stiffness of the material, and, in its simplest form, the fractional reduction in stiffness can be represented by a scalar damage index, d, which is 0 for material in an undamaged state, and can evolve to a maximum value of 1 for fully damaged material. The effective stiffness tensor, $\tilde{E}$, is computed by scaling down the original stiffness tensor, E:

$$\tilde{E} = (1 - d)E \tag{7}$$

For linearly elastic material, the effective stress, $\tilde{\sigma}$, is computed from the strain, ϵ, as:

$$\tilde{\sigma} = \tilde{E}\epsilon = (1 - d)E\epsilon \tag{8}$$

This concept can be similarly applied to other constitutive models by scaling the stress computed by the constitutive model, σ, which may already account for material and geometric nonlinearities, to compute an effective stress that accounts for damage:

$$\tilde{\sigma} = (1 - d)\sigma \tag{9}$$

Equilibrium is enforced using the effective stress tensor in the same manner that it would typically be enforced using the standard stress tensor.

The decrease in stiffness (manifested as a decrease in the stress under a given strain) due to damage in CDM is similar to the effect of thinning due to wastage in the metallic fuel cladding that needs to be captured in the mechanical response. The stiffness of the cladding should decrease due to wastage, and, under a given hoop strain, the integrated hoop stress should

decrease proportionally with the thinning. Thus, the concept of a damage index is applied here to represent the effect of wastage on the mechanical response of the cladding. The original cladding geometry is retained, but Equation 9 is applied to compute an effective stress, where d in this case is the ratio of the wastage thinning to the original cladding thickness. The mechanics modules in the MOOSE framework that BISON is based on already has a generic scalar damage capability. A new material model (MetallicFuelWastageDamage) was developed to convert the wastage thinning of the cladding material from FCCI and chemical thinning from CCCI into a fractional damage index, which is then used to compute an effective stress that is used in mechanical equilibrium enforcement. The apparent stiffness of the thinned cladding decreases, which, under the same internal pressurization, results in higher strain, stress, and creep rate. This allowed for the extra creep caused from FCCI and CCCI to be modeled for experiment X447/X447A. It should be noted that this method only affects the mechanical response. Thermally, the cladding behaves as if it had its original thickness, which is a reasonable approximation because of the relatively high thermal conductivity of the cladding.

2.5 Optimization

The optimization uses a genetic algorithm that, through a process mimicking "natural selection," allows for generations of solutions to be produced and improved with each successive generation. By making changes in adjustable parameters, batches, or generations, of potential optimized points are produced. These are referred to as individuals, from a seed, or parent individual. Each generation creates 200 individuals, each containing an associated BISON job to be performed. The first parent individual has a friction coefficient value of 0.5, an anisotropic swelling coefficient of 0.5, and an HT9 creep first thermal scalar of 1. This point was selected as it represented a position centered in the bounds of the potential values of investigation and was the default value within the HT9 creep model. From the first individual, another 200 sets of variables were generated. The new variables are produced using Python's native random number generators coupled with a mutation factor supplied by the algorithm. The purpose of the mutation factor is to ensure that there is a strong convergence by representing the maximum mutation possible for any child from its parent. With each generation, the mutation factor will become smaller as a function of the difference between the individual's position and its parent's position. The smallest mutation allowable is equal to 0.01 for both the friction and anisotropic swelling factor, with the first thermal scalar limited to integers only. After a new generation is created, all of the new individual's variables are sent through BISON for calculation.

The three parameters of profilometry, axial swelling, and CDF are calculated from the BISON output files then fed back into the optimization as individuals. To evaluate the cladding profilometry fit between BISON and PIE data, the standard error of the estimate (SEE) was used. This method is illustrated in Figure 3 and Equation 10. SEE was chosen to evaluate the BISON cladding profilometry as it takes into account the axial shift of the profiles by accounting for the differences between the two sets of data, as shown in Equation 10, where y is the BISON clad displacement, $\hat{y}$ is the PIE clad displacement, and n is the number of profilometry datapoints in a pin [30][31]. Axial fuel swelling and CDF estimated by BISON were compared to PIE values and known pin failures to estimate the error and failure predictions.

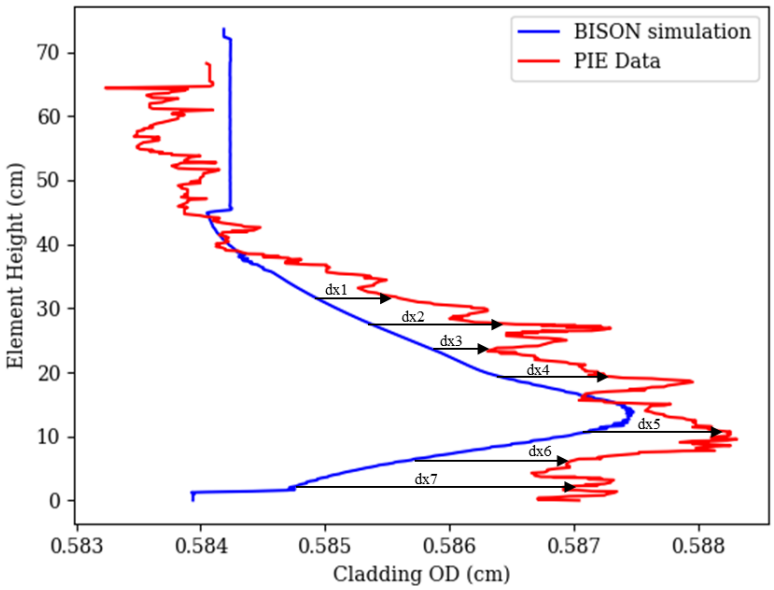

Figure 3. Profilometry profile statistical assessment with SEE [4].

$$SEE = \sqrt{\frac{\sum(y - \hat{y})^2}{n - 2}} \tag{10}$$

The composite magnitude of the SEE and axial fuel swelling error are calculated using standard Euclidean methods shown in Equation 11, where p_1 and p_2 are the error of the two parameters. In the case for CDF, no error is assigned due to the variation of CDF values generated from BISON. The genetic optimization is optimizing the composite magnitude in Equation 11. For each simulation generated by the genetic algorithm, the magnitude is computed and assigned to the individual. After calculating the magnitude, the individuals are then pushed to a minimizing priority heap. The top 10 simulations with the lowest composite magnitude are labeled as survivors and become the parents of the next generation. Each of the survivors then generates 20 children for the next generation through mutation.

$$M = \sqrt{{p_1}^2 + {p_2}^2} \tag{11}$$

The mutation and generation of new individuals is handled by a mutation function which produces a mutation factor (MF) for every new parent. The MF is critical to aid the convergence of the genetic algorithm. The MF represents the greatest possible mutation of variables a child can inherit from a parent. With each successive generation, the MF becomes smaller. By becoming smaller, the MF allows for much more focused search parameters and better convergence. The MF is what differentiates a genetic algorithm from a parametric study. The MF calculation used in this work is shown in Equation 12. The MF of a child is going to be equivalent to the difference between a parent's variables and a child's variables. Each generation will provide a smaller MF value with the smallest allowed MF being 0.01.

$$MF_{max} = |Parent_{var} - Child_{var}| \tag{12}$$

New generations will continue to be generated until one of several conditions are met. The first stoppage criteria is when the iterative error in Equation 13 is below 0.001. The second stoppage criteria is to keep track of recurring optimal solutions. If an individual is selected five times as the most optimal solution, it will be returned as the optimal individual to avoid infinite

looping. The optimization of the friction coefficient and anisotropic swelling factor was optimized for Pin DP11 in experiments X447 and X447A before being used to evaluate other pins within those experiments.

$$E = \left| \frac{x_{old} - x_{new}}{x_{old}} \right| \tag{13}$$

The SEE and axial fuel swelling error between the BISON simulations and PIE data were calculated for each pin in X447/X447A. In addition to pin-level statistics, the SEE and axial fuel swelling error were reported for X447/X447A to assess the anisotropic swelling factor, the friction coefficient, and the effect FCCI had on cladding profilometries. A single value for SEE for the X447/X447A experiments was reported along with the average axial fuel swelling error and corresponding standard deviation. Note that creep is included in the cladding diameter change for both modeling and PIE data, the variability of which could affect the differences between the two in addition to differences caused from FCCI.

3. RESULTS AND DISCUSSION

The optimal friction coefficient, anisotropic swelling factor, and HT9 first thermal creep scalar for all pins within X447/447A were found to contain multiple combinations that yield the same composite error magnitude, particularly the friction coefficient. Varying the friction coefficient between the fuel and the cladding had no significant change in the axial fuel swelling height above a friction value of 0.2, with the anisotropic fuel swelling factor and HT9 first thermal creep scalar being the major influence over the BISON-simulated cladding profilometry and the axial fuel swelling height results. It's important to note that the anisotropic swelling factor doesn't influence the SEE of X447/447A pins, as the SEE value is being driven by the main peak caused by thermal creep, and the effects of FCCI on the cladding for X447/X447A. The anisotropic swelling factor and HT9 first thermal creep scalar used for all X447/447A pins contained were an optimal friction coefficient of 0.2, an anisotropic swelling factor of 0.20, and a HT9 first thermal creep scalar of 17. Figure 4 shows DP11 cladding profilometry simulated with these parameters. This combination yielded the lowest X447/X447A experiment SEE value being 17.7 μm, and the lowest error metric being 206 μm.

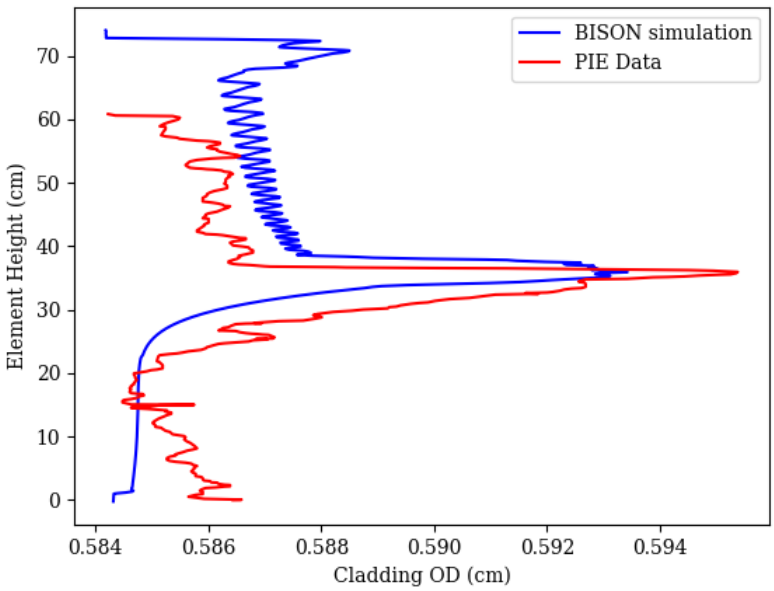

Figure 4. X447A DP11 cladding profilometry with a 0.2 friction coefficient, 0.2 anisotropic swelling factor, and 17 HT9 first thermal creep scalar.

The oscillations that occur above the top of the EBR-II fuel in Figure 4 are an artifact due to the mesh size chosen for modeling efforts. The sizing of the mesh can bring numerical instability and imperfect numerical convergence due to the PDE

solvers utilized in the thermal contact action within BISON and MOOSE [28][29]. This is seen in the outer cladding wall temperature profile as well. The main peak at ~35 cm is caused by the coupling of FCCI back into the BISON model through the tensor mechanics action using a damage model and the HT9 first thermal creep scalar. This is due to the elevated cladding temperatures at the top of the fuel pin where FCCI and thermal creep is more likely to occur. The elevated temperatures seen throughout X447/X447A are due to the decreased flowrate of the sodium coolant. Unfortunately, Experiment X447 does not have any cladding profilometry available in FIPD for comparison. The SEE value for pin DP11 in X447 as found to be 17.7 µm, which is comparable to previous work [4]. The axial fuel swelling length of DP11 was compared to the axial fuel swelling PIE values found within FIPD, with the difference being 65 µm for X447. This is a significant improvement in axial fuel swelling length predictions when compared to previous work [3][4]. The main cause for this is the use of a higher anisotropic swelling factor and a lower terminating porosity value than the BISON default.

The optimal anisotropic swelling factor for all pins in X447/X447A was found to be 0.20. This value is significantly lower than the anisotropic swelling factor found in previous literature for U-10Zr fuel, being 0.28 and 0.4, respectively [21][23]. This lower anisotropic value was needed due to fuel swelling being fixed by the terminating porosity value within the BISON UPuZrGaseousEigenstrain model with additional swelling from solid fission products being added. Using a terminating porosity value of 0.19 allows for each X447/X447A fuel slug to swell 23.5 % with 1.5% additional swelling for each at.% burnup. This led to an underprediction of axial fuel swelling for low burnup pins (~4.75 at.%) and an overprediction of higher burnup pins (~8.5 at.%), with the axial fuel swelling length difference of all pins in X447/X447A averaging –207 µm. This presents the need for a hot-pressing model for metallic fuel in BISON that is similar to ALFUS to counteract overpredictions of fuel swelling seen. This would also allow for a higher terminating porosity to be used to better predict profilometry and fuel swelling at lower burnups [21][23]. Lowering the anisotropic factor below values presented in previous work allowed for the axial fuel swelling to be in better agreement with PIE measurements without changing the SEE for the X447/447A pins significantly, as the anisotropic factor doesn't affect the magnitude of the main thermal creep peak.

The statistical fitting for experiment X447/447A shows agreement for U-10Zr fuel with both HT9 and D9 cladding for different burnups at elevated temperatures for cladding profilometry and axial fuel swelling measurements. D9 clad pin C717 shows good cladding profilometry agreement with PIE measurements in Figure 5. However, the standard deviation of the average axial fuel swelling difference was 0.48 cm. This is due to the current models and physics used in BISON modeling fuel swelling only due to fission gas production and solid fission product buildup. Fuel swelling due to fission gas production leads to a fixed fuel swelling volume with solid fission fuel swelling adding to this value. This leads to an underprediction of lower burnup pins (~4.5 at. % BU) and an overprediction of higher burnup pins (~8.9 at. % BU). Due to SEE values of pins being orders of magnitudes lower than axial fuel swelling errors, the affect SEE values have on the error metric in Table 2 is insignificant.

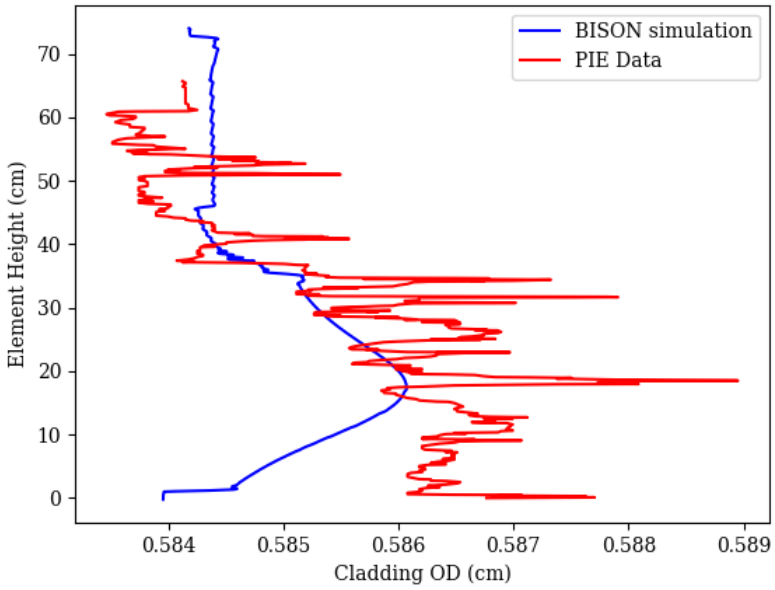

Figure 5. X447A C717 (D9) cladding profilometry with a 0.2 friction coefficient and 0.2 anisotropic swelling factor.

Table 2. Experiment X447/447A results with a 0.2 friction coefficient and 0.2 anisotropic swelling factor.

Pin	Sub-Experiment	Error Metric (cm)	SEE (cm)	Axial Growth Error (cm)	CDF
C627	X447	4.1E-01	N/A	-4.1E-01	1.1E-03
C627	X447A	3.5E-01	1.5E-03	3.5E-01	2.3E-03
C628	X447	6.8E-01	N/A	-6.8E-01	1.1E-03
C628	X447A	8.4E-02	1.9E-03	8.4E-02	2.0E-03
C629	X447	6.6E-01	N/A	6.6E-01	9.5E-04
C629	X447A	1.3E-01	2.2E-03	-1.3E-01	2.7E-03
C630	X447	2.1E-01	N/A	-2.1E-01	2.5E-05
C630	X447A	6.7E-01	1.5E-03	6.7E-01	3.3E-05
C631	X447	2.8E-01	N/A	-2.8E-01	8.7E-04
C631	X447A	4.6E-01	1.7E-03	4.6E-01	2.7E-03
C634	X447	6.4E-01	N/A	-6.4E-01	1.4E-03
C634	X447A	4.5E-02	1.3E-03	4.5E-02	1.4E-03
C639	X447	3.3E-01	N/A	-3.3E-01	3.2E-05
C639	X447A	6.2E-01	1.3E-03	6.2E-01	3.6E-05
C640	X447	7.4E-01	N/A	-7.4E-01	1.7E-05
C640	X447A	4.2E-02	1.3E-03	-4.2E-02	5.6E-05
C641	X447	8.3E-01	N/A	-8.3E-01	3.7E-05
C641	X447A	1.4E-01	1.9E-03	1.4E-01	4.0E-05
C643	X447	7.3E-01	N/A	-7.3E-01	3.7E-05
C643	X447A	1.0E-01	1.6E-03	1.0E-01	4.0E-05
C645	X447	5.6E-01	N/A	-5.6E-01	1.3E-03
C645	X447A	5.0E-02	2.1E-03	5.0E-02	1.3E-03
C652	X447	7.8E-01	N/A	-7.8E-01	1.1E-03
C652	X447A	1.3E-01	1.2E-03	-1.3E-01	1.3E-03
C655	X447	5.1E-01	N/A	-5.1E-01	1.3E-03
C655	X447A	7.2E-02	2.4E-03	7.2E-02	1.3E-03
C659	X447	4.0E-01	N/A	-4.0E-01	2.0E-05
C659	X447A	3.8E-01	2.6E-03	3.8E-01	5.0E-05
C661	X447	4.8E-01	N/A	-4.8E-01	1.1E-03
C661	X447A	7.7E-02	1.1E-03	7.7E-02	1.5E-03
C664	X447	7.4E-01	N/A	-7.4E-01	1.7E-05
C664	X447A	1.0E-01	1.9E-03	1.0E-01	3.7E-05
C668	X447	4.5E-01	N/A	-4.5E-01	3.6E-05
C668	X447A	2.0E-01	1.8E-03	2.0E-01	3.8E-05
C674	X447	6.4E-01	N/A	-6.4E-01	1.5E-03
C674	X447A	2.8E-02	1.8E-03	-2.8E-02	1.5E-03
C677	X447	5.6E-01	N/A	-5.6E-01	1.0E-03
C677	X447A	7.8E-02	1.8E-03	7.8E-02	1.0E-03
C686	X447	2.4E-01	N/A	2.4E-01	1.4E-03
C686	X447A	8.3E-01	1.6E-03	8.3E-01	1.4E-03
C688	X447	2.9E-01	N/A	-2.9E-01	7.6E-04
C688	X447A	3.3E-01	1.5E-03	3.3E-01	3.2E-03
C689	X447	5.7E-01	N/A	-5.7E-01	1.0E-03
C689	X447A	1.0E-01	1.9E-03	1.0E-01	2.1E-03
C698	X447	1.8E-01	N/A	1.8E-01	3.0E-05
C698	X447A	7.0E-01	1.8E-03	7.0E-01	3.5E-05
C702	X447	6.3E-01	N/A	-6.3E-01	1.1E-03
C702	X447A	5.2E-02	1.6E-03	-5.1E-02	1.1E-03
C707	X447	6.3E-01	N/A	-6.3E-01	2.0E-05
C707	X447A	1.4E-01	1.6E-03	1.4E-01	5.6E-05
C709	X447	4.1E-01	N/A	-4.1E-01	9.6E-04
C709	X447A	2.3E-01	1.4E-03	2.3E-01	2.7E-03

C710	X447	7.5E-01	N/A	-7.5E-01	1.5E-05
C710	X447A	2.7E-02	2.5E-03	-2.7E-02	5.2E-05
C715	X447	4.3E-01	N/A	4.3E-01	1.8E-05
C715	X447A	1.1E+00	1.9E-03	1.1E+00	6.7E-05
C717	X447	9.8E-02	N/A	9.8E-02	9.5E-04
C717	X447A	7.7E-01	9.7E-04	7.7E-01	1.8E-03
C719	X447	6.1E-01	N/A	6.1E-01	1.1E-03
C719	X447A	1.3E+00	1.7E-03	1.3E+00	1.9E-03
DP02	X447	5.0E-01	N/A	-5.0E-01	1.8E-04
DP02	X447A	3.9E-01	1.4E-03	3.9E-01	3.4E-03
DP03	X447	4.5E-01	N/A	-4.5E-01	5.0E-04
DP04	X447	4.3E-01	N/A	-4.3E-01	2.5E-04
DP04	X447A	5.8E-01	1.6E-03	5.8E-01	7.9E-03
DP06	X447	2.5E-01	N/A	-2.5E-01	5.0E-04
DP07	X447	5.9E-01	N/A	-5.9E-01	3.7E-04
DP07	X447A	3.4E-01	1.8E-03	3.4E-01	4.0E-03
DP09	X447	4.7E-01	N/A	-4.7E-01	2.4E-04
DP09	X447A	3.7E-01	1.2E-03	3.7E-01	1.1E-03
DP10	X447	7.8E-01	N/A	-7.8E-01	9.1E-05
DP10	X447A	8.5E-02	1.4E-03	8.5E-02	3.3E-03
DP11	X447	6.5E-02	N/A	6.5E-02	6.4E-04
DP11	X447A	1.0E+00	1.8E-03	1.0E+00	5.4E-03
DP12	X447	5.6E-01	N/A	-5.6E-01	7.7E-05
DP12	X447A	3.0E-01	8.8E-04	3.0E-01	3.8E-03
DP13	X447	3.3E-01	N/A	-3.3E-01	4.5E-04
DP13	X447A	5.8E-01	1.4E-03	5.8E-01	2.6E-03
DP14	X447	3.1E-01	N/A	-3.1E-01	4.2E-04
DP14	X447A	6.0E-01	9.0E-04	6.0E-01	2.2E-03
DP57	X447A	2.1E-01	8.3E-04	2.1E-01	5.4E-04
DP66	X447	4.4E-01	N/A	-4.4E-01	3.0E-04
DP66	X447A	4.1E-01	N/A	4.1E-01	3.4E-03
DP69	X447	1.4E-01	N/A	-1.4E-01	2.4E-04
DP70	X447	3.3E-01	N/A	-3.3E-01	1.7E-04
DP70	X447A	5.3E-01	N/A	5.3E-01	8.6E-03
DP71	X447A	2.3E-02	8.8E-04	2.3E-02	9.9E-04
DP72	X447	6.1E-01	N/A	-6.1E-01	6.4E-05
DP72	X447A	3.3E-01	1.3E-03	3.3E-01	3.1E-03
DP75	X447	3.5E-01	N/A	-3.5E-01	2.6E-04
DP75	X447A	5.9E-01	N/A	5.9E-01	5.1E-03
DP76	X447	3.9E-01	N/A	-3.9E-01	1.8E-04
DP76	X447A	3.6E-01	1.0E-03	3.6E-01	1.8E-03
DP77	X447	2.0E-01	N/A	-2.0E-01	3.4E-04
DP77	X447A	7.4E-01	1.3E-03	7.4E-01	1.6E-03
DP80	X447A	3.9E-02	9.7E-04	3.9E-02	5.7E-04
DP81	X447	1.7E-02	N/A	-1.7E-02	2.5E-04
DP83	X447A	1.2E-01	6.1E-04	1.2E-01	6.4E-04
All Pins	Both	2.1E-02	-7.7E-04	-2.1E-02	1.2E-03
All Pins STD	N/A	2.7E-01	4.5E-04	4.9E-01	1.6E-03

The implementation of coupling FCCI back into the BISON model by inducing extra stress from a damage fraction within the tensor mechanics action in BISON was found to sufficiently describe the phenomena in X447/447A profilometry for high temperature HT9 and D9 pins coupled with adjusting the HT9 first thermal creep scalar. The FCCI is modeled by increasing the stress in the cladding due to cladding wastage without actually changing cladding thickness. This implementation improves the BISON profilometry results to better match and describe the PIE profilometry. Coupling FCCI through the use of a ComputeMultipleInelasticStress damage model was applied to colder pins outside of the X447/447A bundle and was found to not change previous modeling results that didn't contain this coupling. Adjusting the HT9 first thermal creep scalar was found to give better PIE profilometry agreement with BISON results without impacting the profilometry results of colder pins outside

of the inner, hotter X447/X447A bundle. However, it was observed that the implementation of FCCI coupling and adjusting the HT9 first thermal creep scalar for X447/447A pins both underpredicted and overpredicted the main peak within the PIE profilometry. An underprediction of the main peak is seen in Figure 6 and primarily occurred in the inner row or ring of HT9 pins (denoted in Figure 8) and an overprediction occurring in the outer ring, as seen in Figure 7.

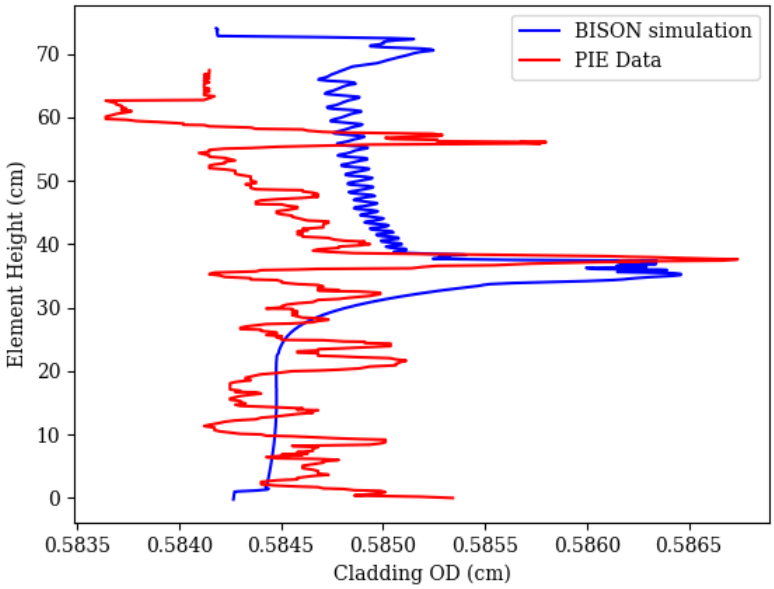

Figure 6. X447A DP83 cladding profilometry with a 0.2 friction coefficient, 0.2 anisotropic swelling factor, and 17 HT9 first thermal creep scalar.

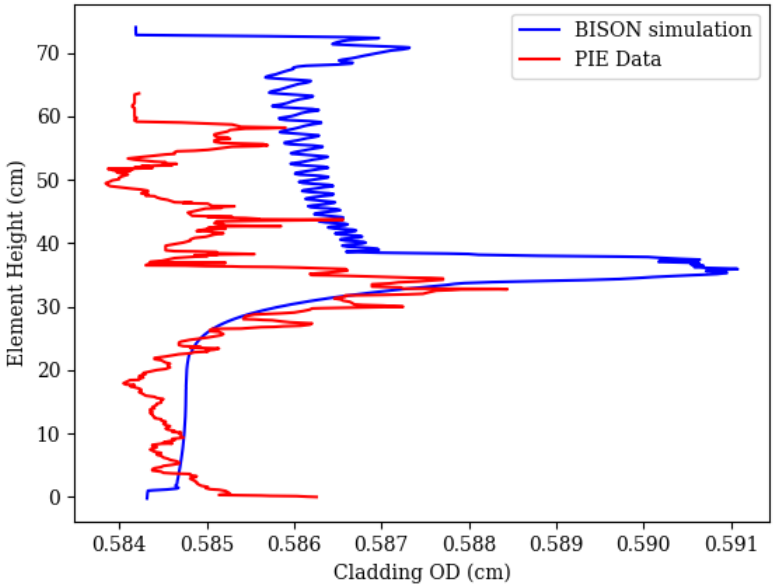

Figure 7. X447A DP07 cladding profilometry with a 0.2 friction coefficient, 0.2 anisotropic swelling factor, and 17 HT9 first thermal creep scalar.

It is believe that this discrepancy is due to an irregularity within the X447/447A fuel pins not coupling in thermal feedback from neighboring pins and the FCCI empirical correlations being based off PIE results from X447A [8][9]. The inclusion of

dummy pins in X447/447A, denoted by 'X' in Figure 8, allows for the D9 pins to operate at cooler temperatures due to an increased cooling capacity. This effect is carried over to the outer HT9 pins, allowing them to run cooler than the HT9 pins in the middle of the assembly. Not taking neighboring pins into account within the BISON modeling directly affects the simulated profilometry, as the empirical correlations used to model FCCI and thermal creep are temperature dependent. Neighboring pins being accounted for would lead to lowering cladding temperatures, wastage thickness, and thermal creep accelerated by FCCI. The PIE profilometry results support this, as the HT9 pins within the inner highlighted ring in Figure 8 show more cladding strain than the pins in the outer highlighted ring.

To account for neighboring pins in a single fuel pin simulation, the heated perimeter, flow area, and coolant LHGR were adjusted within the coolant channel model dependent on assembly position to account for the dummy pins. However, thermal feedback from neighboring pins was not taken into account for the conducted BISON simulations. The maximum coolant temperatures produced within BISON were within 3 K of the values within FIPD for all pins within X447/X447A. This directly affected all C-series pins within X447/447A and the outer DP-series pins. This implementation only needs to be done for assemblies containing dummy pins or assemblies with mixed flowrates, such as X447/447A. C-series D9 pins within X447A did not have a significant change when coupling FCCI into BISON simulations, as the wastage thinning of D9 cladding isn't significant at peak temperatures within X447/447A. This would lead to more cladding strain on one side of the pin and may have contributed to DP70 and DP75 failing and the underprediction of cladding profilometries. Within the BISON simulations, pin failure was not modeled with failure implications feeding back into modeling parameters, such as stress cracking.

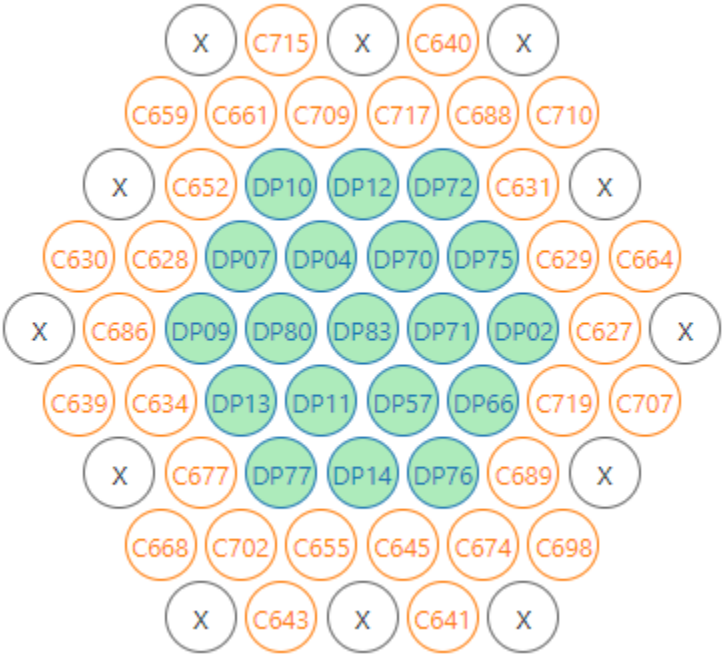

Figure 8. X447A assembly loading diagram.

The two pins in X447A that were known to have failed were DP70 and DP75. Both of these failures were due to FCCI accelerating thermal creep and crack growth within the cladding wall. However, each of these pins modeled within BISON did not predict cladding rupture using CDF correlations, which is a function of temperature and stress. CDF values for all pins are seen in Table 1. Although the stress induced by the FCCI coupling with ComputeMultipleInelasticStress was greater than the base simulation, the CDF values from BISON were not sufficient to declare pin failure. In contrast, pins known to have not failed, such as DP11, predicted higher CDF values within the BISON simulations. Although CDF is only a probability of pin failure, the probability that none of the pins using BISON CDF values is 88.7%, and 0.0039% that only DP70 and DP75 failed. This value is unrealistically low when knowing the outcome of the X447/447A experiments, with multiple other pins being close to failure. This inaccuracy is why other means should be used to evaluate pin failure probability, such as cladding strain. Possible causes for this include the lack of stress due to the anisotropic and terminating porosity values used during these simulations. Increasing the terminating porosity and anisotropic swelling factor in such a way as to still predict the same axial fuel swelling height would yield more stress in the cladding, increasing CDF values. However, this would cause cladding profilometry to be overpredicted unless a U-Pu-Zr hot pressing model, with Pu being zero, was added to the BISON code. A

U-Pu-Zr hot pressing model would allow for FCMI to occur sooner within the BISON simulations without overpredicting the stress within the cladding.

The friction coefficient and anisotropic swelling factor used within this study were similar to previous work, and used to model pins within X441, X486, and X421 with lower cladding temperatures than X447 [4]. These two parameters yielded similar FCMI results for lower temperature pins, as gaseous fuel swelling past terminating porosity is not temperature dependent. Adjusting the HT9 first thermal scalar from 1 to 17 allowed for better agreement between the BISON and PIE cladding profilometry for high temperatures pins within X447/447A. Due to the first term within the HT9 thermal creep equation being driven mainly by temperature, the impact the first term will have on creep and cladding strain with a 50 K temperature drop is minimum due to the second term of the HT9 thermal creep equation and irradiation creep contributing significantly more creep strain. With this in mind, applying the optimal friction coefficient, anisotropic swelling factor, and HT9 first thermal scalar to colder metallic fuel pins are applicable and yield good agreement with PIE cladding profilometry measurements. This is seen in Figure 9 below for pin DP21 from X441A.

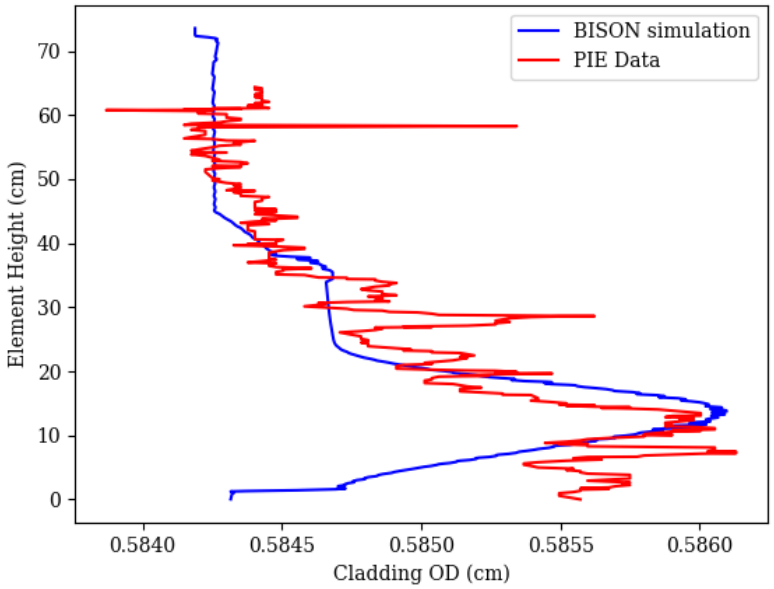

Figure 9. X441A DP21 cladding profilometry with a 0.2 friction coefficient, 0.2 anisotropic swelling factor, and 17 HT9 first thermal creep scalar.

4. CONCLUSIONS

Experiment X447/X447A within EBR-II was modeled with the BISON fuel performance code to assess PIE axial swelling height and cladding profilometry measurements. Due to the higher temperatures of X447/X447A caused by a reduced flowrate and elevated temperatures, FCCI needed to be coupled within the simulations to account for increased cladding creep. Three different parameters within the BISON simulations were optimized to fit the axial swelling height and cladding profilometry measurements for all available pins within X447/X447A. The three parameters are the anisotropic swelling factor, FCMI friction coefficient, and the HT9 first thermal creep scalar. It was found that FCMI with a friction coefficient greater than 0.2 yielded the same error metric with the other two parameters fixed and helped limit the axial growth of the fuel. The optimal anisotropic swelling factor was determined by fitting the BISON axial swelling results to the PIE axial fuel swelling measurements found in IMIS and FIPD. The standard deviation when comparing the difference between BISON axial fuel height results and PIE measurements for pins in X447/X447A was 0.48 cm, which is significantly more than the average difference of –207 µm. This is due to the BISON simulations underpredicting axial swelling at low burnups and overpredicting at higher burnups. An implementation of a U-Pu-Zr hot pressing model would allow for higher terminating porosity and anisotropic swelling factors to be used to better match PIE axial swelling measurements at all burnups without exceeding cladding strain profilometry measurements. To optimize the main peak present within the X447/X447A cladding profilometry data, FCCI was included in the BISON simulations in addition to adjusting the HT9 first thermal creep scalar. This led to decreasing the SEE values and the error metric for each pin and the experimental SEE value and error metric. Although the

HT9 thermal scalar was adjusted to match X447/447A pins, the same optimized parameters need to be applied to other EBR-II pins evaluate fuel performance predictions. In addition to this, models describing hot pressing of U-Pu-Zr fuel should be included to address the overprediction of cladding strain due to FCMI. Using pin data within the IMIS and FIPD databases allows material models within BISON to be validated by comparing simulation results to PIE measurements with the optimized parameters. This allows for different parameters within current models, such as in this work, to be optimized and used to predict fuel performance of future reactors being designed.

Funding: This research was funded by INL LDRD 19A39-103FP.

Institutional Review Board Statement: Not Applicable

Informed Consent Statement: Informed consent was obtained from all subjects involved in the study.

Data Availability Statement: Data available on request due to restrictions (e.g., privacy or ethical). The data presented in this study are available on request from the corresponding author. The data are not publicly available due to export control.

Acknowledgments: I would like to acknowledge Adam X. Zabriskie, Stephen R. Novascone, Aaron Oaks, and Abdellatif Yacout for providing review input, knowledge, and experimental data.

Conflicts of Interest: The authors declare no conflict of interest.

REFRENCES

[1] D. C. Crawford, L. Steven, and J. J. Powers, "A Proposed Startup Fuel for the Versatile Test Reactor," *Trans. Am. Nucl. Soc.*, vol. 118, no. June 17-12, 2018.

[2] R. L. Williamson *et al.*, "BISON : A Flexible Code for Advanced Simulation of the Performance of Multiple Nuclear Fuel Forms," *Nucl. Technol*, 2021, doi: https://doi.org/10.1080/00295450.2020.1836940.

[3] K. M. Paaren, M. Gale, M. J. Kerr, P. G. Medvedev, and D. L. Porter, "Initial demonstration of Automated fuel performance modeling with 1,977 EBR-II metallic fuel pins using BISON code with FIPD and IMIS databases," *Nucl. Eng. Des.*, 2021.

[4] K. M. Paaren, N. Lybeck, K. Mo, P. G. Medvedev, and D. L. Porter, "Cladding Profilometry Analysis of EBR-II metallic fuel pins with HT9, D9, and SS316 cladding," *Energies*, 2021.

[5] G. L. Hofman, M. C. Billone, J. F. Koenig, and J. M. Kramer, "Metallic Fuels Handbook," 2019 [Online]. Available: https://publications.anl.gov/anlpubs/2019/04/151709.pdf

[6] D. D. Keiser, "Fuel cladding chemical interaction in metallic sodium fast reactor fuels: A historical perspective," *J. Nucl. Mater.*, vol. 514, pp. 393–398, 2019, doi: 10.1016/j.jnucmat.2018.09.045. [Online]. Available: https://doi.org/10.1016/j.jnucmat.2018.09.045

[7] C. Matthews, C. Unal, J. Galloway, D. D. Keiser, and S. L. Hayes, "Fuel-cladding chemical interaction in U-Pu-Zr metallic fuels: A critical review," *Nucl. Technol.*, vol. 198, no. 3, pp. 231–259, 2017, doi: 10.1080/00295450.2017.1323535. [Online]. Available: https://doi.org/10.1080/00295450.2017.1323535

[8] J. D. Hales *et al.*, "BISON Users Manual - BISON Release 1.2," Idaho Falls, 2015 [Online]. Available: https://bison.inl.gov/SiteAssets/BISON_users_version_1_2.pdf

[9] W. J. Carmack, "Temperature and Burnup Correlated Fuel-Cladding Chemical Interaction in U-10Zr Metallic Fuel," University of Idaho, 2012 [Online]. Available: http://dx.doi.org/10.1016/j.jaci.2012.05.050

[10] S. R. Novascone, A. Casagranda, P. G. Medvedev, C. Matthews, and A. X. Zabriskie, "Summary and Assessment of Metallic Fuel Capabilities in Bison," *Idaho Natl. Lab. Rep.*, no. September, p. INL/EXT-18-51399, 2018.

[11] A. M. Kim, Yeon Soo and Hayes, S L and Hofman, G L and Yacout, "Modeling of constituent redistribution in U-Pu-Zr metallic fuel," *J. Nucl. Mater.*, vol. 359, no. 1–2, pp. 17–28, 2006.

[12] M. C. Billone, Y. Y. Liu, E. E. Gruber, T. H. Hughes, and J. M. Kramer, "Status of Fuel Element Modeling Codes for Metallic Fuels," in *Proceedings American Nuclear Society Internaionl Conference on Reliable Fuels for Liquid Metal Reactors*, 1968.

[13] H. Savage, "The heat content and specific heat of some metallic fast-reactor fuels containing plutonium," *J. Nucl. Mater.*, vol. 25, no. 3, pp. 249–259, 1968, doi: 10.1016/0022-3115(68)90168-2.

[14] N. Yamanouchi, M. Tamura, H. Hayakawa, and T. Kondo, "Accumulation of engineering data for practical use of reduced activation ferritic steel: 8%Cr-2%W-0.2%V-0.04%Ta-Fe," *J. Nucl. Mater.*, vol. 191–194, pp. 822–826, 1992.

[15] A. Banerjee, S. Raju, R. Divakar, and E. Mohandas, “High Temperature Heat Capacity of Alloy D9 Using Drop Calorimetry Based Enthalpy Increment Measurements,” *Int. J. Thermophys.*, vol. 28, no. 1, pp. 98–108, 2007.
[16] L. Leibowitz and R. A. Blomquist, “Thermal conductivity and thermal expansion of stainless steels D9 and HT9,” *Int. J. Thermophys.*, vol. 9, pp. 873–883, 1988.
[17] Kenneth C. Mills., *Recommended Values of Thermophysical Properties for Selected Commercial Alloys*. Woodhead Publishing, 2002 [Online]. Available: http://app.knovel.com/hotlink/toc/id:kpRVTPSCA1/recommended-values-thermophysical/recommended-values-thermophysical
[18] D. R. Olander, *Fundamental aspects of nuclear reactor fuel elements*. Technical Information Center, Energy Research and Development Administration, 1976.
[19] Los Alamos National Laboratory, “AFCI Materials Handbook, Materials Data for Particle Accelerator Applications, Chapter 18 - Design Properties of HT9 and Russian Ferritic/Martensitic Steels, Rev 6,” 2014.
[20] K. J. GeelHood and I. E. Porter, “Modeling and Assessment of EBR-II Fuel with the US NRC’s Fast Fuel Performance Code,” in *Proceedings of Top Fuel*, 2018, p. 12 [Online]. Available: https://www.euronuclear.org/archiv/topfuel2018/fullpapers/TopFuel2018-A0115-fullpaper.pdf
[21] A. Karahan, “Modeling of thermo-mechanical and irradiation behavior of mixed oxide fuel for sodium fast reactors,” Massachusetts Institute of Technology, 2010 [Online]. Available: https://core.ac.uk/download/pdf/4422038.pdf
[22] G. L. Hofman, L. C. Walters, and T. H. Bauer, “Metallic Fast Reactor Fuels,” *Prog. Nucl. Energy*, vol. 31, no. 1, pp. 83–110, 1997, doi: 10.1017/CBO9781107415324.004.
[23] T. Ogata and Y. Takeshi, “Development and Validation of ALFUS: An Irradiation Behavior Analysis code for Metallic Fast Reactor Fuels,” *Nucl. Technol.*, vol. 128, pp. 113–124, 1999, doi: 10.2514/5.9781600866081.0755.0814.
[24] A. Karahan and J. Buongiorno, “A new code for predicting the thermo-mechanical and irradiation behavior of metallic fuels in sodium fast reactors,” *J. Nucl. Mater.*, vol. 396, pp. 283–293, 2010.
[25] L. L. Briggs, Y. Il Chang, and D. J. Hill, “Safety Analysis and Technical Basis for Establing an Interim Burnup Limit for Mark-V and Mark-VA Fueled Subassemblies in EBR-II,” 1995 [Online]. Available: https://www.osti.gov/servlets/purl/1542889
[26] A. M. Yacout, A. Oaks, W. Mohamed, and K. Mo, “FIPD : EBR-II Fuels Irradiation & Physics Database,” 2017 [Online]. Available: https://publications.anl.gov/anlpubs/2018/08/141545.pdf
[27] A. Oaks, K. Mo, W. Mohamed, and A. Yacout, “Development of FIPD: The EBR-II Fuels Irradiation & Physics Database,” in *Top Fuel 2019: lIght Water Reactor Fuel Performance Conference*, 2019.
[28] J. Lemaitre, “A continuous damage mechanics model for ductile fracture,” *J. Eng. Mater. Technol. Trans. ASME*, vol. 107, no. 1, pp. 83–89, 1985, doi: 10.1115/1.3225775.
[29] J. Lemaitre, *A Course on Damage Mechanics*. Springer, Berlin, Heidelberg, 1992.
[30] B. S. Everitt and A. Skrondal, *The Cambridge Dictionary of Statistics*, 4th ed. New York: Cambridge University Press, 2010.
[31] J. Cohen, *Statistical Power Analysis for the Behavioral Sciences*, 2nd ed. 1988.